Rapid Land Cover Change Detection with Optical and SAR Satellite Data after Tropical Cyclone Seroja - Case Study in Dili, Timor-Leste

Pedro J.F. [1*], Masahiko N.[1,2]

[1]Graduate School of Science and Technology for Innovation, Yamaguchi University, 2-16-1, Ube 755-8611, Yamaguchi, Japan

[2]Center for Research and Application of Satellite Remote Sensing, Yamaguchi University, 2-16-1, Tokiwadai, Ube 755-8611, Yamaguchi, Japan.

d002wdu@yamaguchi-u.ac.jp

Abstract: *This study utilizes optical PlanetScope imagery and Synthetic Aperture Radar (SAR) data from Sentinel-1 to assess land cover changes in Dili, Timor-Leste, following Tropical Cyclone Seroja. The primary aim is to investigate how combining these data types enhances disaster monitoring and response in areas affected by flooding. Using the Random Forest classifier, known for its effectiveness with high-dimensional and noisy datasets, we categorized land cover into six classes: vegetation, water, built-up areas, bare soil, clouds, and shadows. This categorization was conducted across pre-disaster, post-disaster, and recovery phases using Google Earth Engine (GEE). To improve the delineation of water bodies, we applied binary segmentation through Otsu thresholding on the SAR images. The classification achieved impressive accuracy, with overall accuracy scores ranging from 97% to 98.7% and Kappa indices between 0.947 and 0.968, indicating strong model performance. Notably, the study revealed a significant increase in water bodies, considerable damage to vegetation and built-up areas after the disaster, and a gradual recovery over time. However, challenges were encountered in urban classification, especially in distinguishing between built-up and bare soil areas. This research emphasizes the value of integrating optical and SAR data with machine learning techniques for effective land cover monitoring in post-disaster contexts, contributing to enhanced disaster preparedness, improved recovery planning, and vital insights for managing flood impacts in regions like Timor-Leste, where technical resources and data may be limited.*

Keywords: land cover change; change detection; disaster monitoring; Random Forest classifier; Otsu Thresholding; SAR data; optical imagery; Timor-Leste

Introduction

Tropical cyclones are among the most devastating natural disasters due to the significant rainfall they bring. The heavy precipitation associated with these storms often leads to considerable loss of life and extensive property damage (Klotzbach et al., 2022; Emanuel, 2005; Jing et al., 2024).

In April 2021, Tropical Cyclone Seroja severely impacted Timor-Leste, especially the capital, Dili. Originating near Timor Island, it quickly intensified to Category 3, bringing winds up to 70 knots and waves over 14 meters high. The cyclone resulted in widespread flooding and landslides, damaging infrastructure and disrupting livelihoods across all 13

municipalities, leading to at least 44 fatalities and significant destruction in agriculture, housing, and transportation (Umam et al., 2024; World Bank, 2021). In addition, the cyclone caused significant damage, affecting more than 4,200 hectares of agricultural land and resulting in the loss of around 112,000 livestock. This destruction indicates substantial changes to the land cover and has severely disrupted local agricultural practices. These changes could have long-lasting effects on the region's food security and economic stability (World Bank, 2021). The destruction in Dili highlighted the urgent need for accurate and effective change detection methods across the vast area to assess the extent of damage and support recovery efforts.

In this context, remote sensing technologies have emerged as crucial tools and gained global recognition for their effectiveness in environmental monitoring (Parra, 2022; Wang et al., 2024), particularly in detecting and analyzing land cover changes associated with natural disasters and agricultural practices (Gu & Zeng, 2024; Mashala et al., 2023). Studies highlight Synthetic Aperture Radar (SAR) data in waterbody detection due to its capability to penetrate cloud cover and provide high-resolution imagery, which is crucial for identifying risks and changes in waterbody (Vickers et al., 2019; Lang et al., 2024; Tiampo et al., 2022). Similarly, high-resolution optical satellites are extensively utilized in land cover classification, enabling rapid assessment of land cover changes (Gómez et al., 2016; Vizzari, 2022). These technologies are indispensable for monitoring crop conditions, flood extents, and landslide occurrences, providing crucial data for timely and effective environmental management (Pickering et al., 2021; Al Shafian & Hu, 2024). Despite the proven capabilities of these technologies, there is still a significant gap in their application for detailed post-disaster analysis in Timor-Leste.

This study addresses the challenges of assessing land cover changes in Dili, Timor-Leste, before and after Tropical Cyclone Seroja by utilizing a combination of optical and SAR satellite data. By developing a remote sensing-based change detection framework, this research aims to provide critical insights into the spatial extent of the impacts of heavy rainfall. These insights are essential for enhancing disaster resilience and recovery planning. They will help formulate strategies to improve the preparedness and response capabilities of urban areas facing similar risks.

By focusing on these objectives, the study fills a critical research gap. It provides valuable knowledge to support Dili's recovery and future protection, which could serve as a model for other regions grappling with similar challenges.

Dataset and Study Area

a. PlanetScope Dataset

This research utilizes two primary datasets: Planet Scope optical imagery and Sentinel-1 Synthetic Aperture Radar (SAR) data. Additional GIS data, such as contour lines, streets, amenities, and administrative boundaries, were also employed. The Coordinate Reference System (CRS) used for this study is EPSG:32751 - WGS 84 / UTM zone 51S. Planet Scope Ortho Tile Products, which are radiometrically and sensor corrected, orthorectified, and projected to UTM, were used. The imagery consists of three temporal stages: pre-disaster, post-disaster, and recovery. It covers an area of 24.6 x 16.4 km, with a spatial resolution of 3 x 3 meters and a daily temporal resolution. These exclusively PlanetScope images were acquired through the Planet Explorer website "https://www.planet.com/explorer/(accessed on 16 April 2022)".

Table 1: Characteristics of the PlanetScope Imagery used in this research.

Period	Product name	Acquisition Date	Period
Pre-disaster	011743_32_2262_2021-01-14_BGRN_SR	2021/01/14	3 m
Post-disaster	4355850_5135126_2021-04-09_2403_BGRN_SR	2021/04/09	3 m

b. Sentinel-1 SAR Dataset

Sentinel-1 SAR data is used for water body extraction. The Sentinel-1 satellites provide data with an Interferometric Wide swath mode, double polarization (VV+VH), a swath width of 250 km, and a resolution of 5-20 meters. These Sentinel-1 SAR data were acquired from the Alaska Satellite Facility Data Search website "https://search.asf.alaska.edu/#/(accessed on 16 April 2022)".

Table 2: Characteristics of the Sentinel-1 SAR Imagery used in this research.

Period	Product name	Acquisition Date	Period
Pre-disaster	S1A_IW_GRDH_1SDV_20210312T100017_20210312T100046_036963_045954_F893	2021/03/12	Descending
Post-disaster	S1A_IW_GRDH_1SDV_20210405T100018_20210405T100047_037313_046573_0CA0	2021/04/05	Descending

c. Study area

This study was conducted in Timor-Leste, specifically focusing on its capital city, Dili, located between 8°34'S latitude and 125°34'E longitude as shown in Figure 1. Timor-Leste, officially known as the Democratic Republic of Timor-Leste, is an island nation covering approximately 14,874 km². The climate of Timor-Leste is greatly influenced by the El Niño Southern Oscillation (ENSO), which can modify the timing of the annual rainfall peak and vary the total quantity of rainfall by up to 50% throughout the year (World Bank Group & Asian Development Bank, 2021).

The 24-hour rainfall on April 4, 2021, was almost ten times higher than on any other day during the rainy season, with an average intensity of over 14 millimeters per hour and a peak intensity of over 70 millimeters per hour (Government of Timor-Leste, United Nations, & World Bank, 2021). The rain gauge at Dili's International Airport recorded a staggering 341.8 millimeters of precipitation in just 24 hours. This extreme rainfall caused significant damage through secondary hazards such as flash floods, landslides, and liquefaction, as shown in Figure 2, which were exacerbated by the country's natural topography. Dili City is experiencing rapid population growth and urbanization. This, coupled with inadequate drainage systems and large rivers, exacerbates the city's susceptibility to flooding. With its complex mix of surrounding mountains and smaller lowland regions, Dili's terrain presents a significant challenge in managing floods.

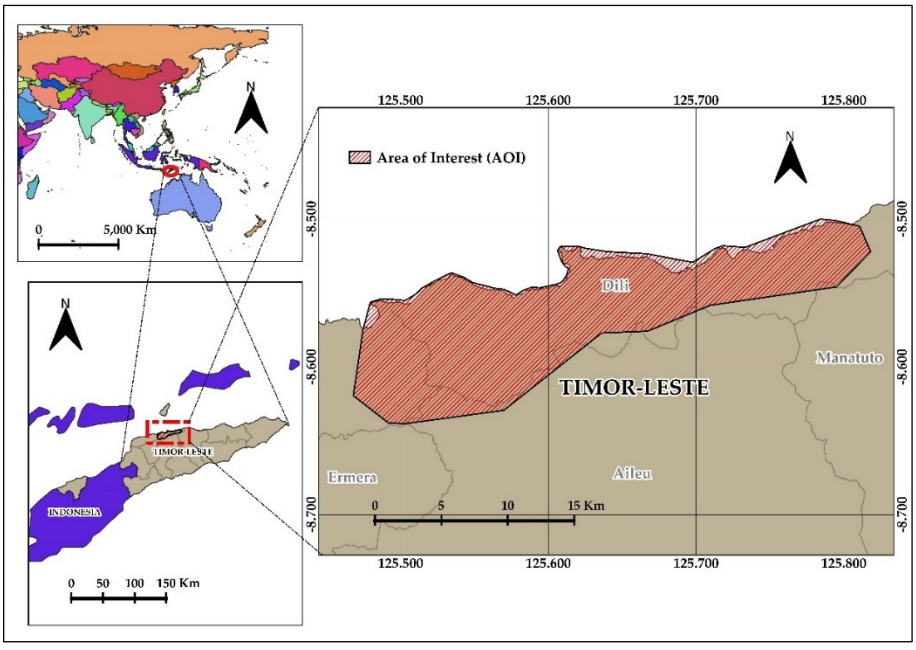

Figure 1: Study Area map showing the most affected city during the disaster.

Figure 2: Flood Impact in Dili, Timor-Leste: Aerial and Ground-Level Visual Documentation.

Methodology

The method proposed for detecting land cover change and delineating flood extents integrates both Sentinel-1 SAR data and PlanetScope optical data, as illustrated in Figure 3. This process involves the following key steps: (a) Access a series of Sentinel-1 SAR Ground Range Detected (GRD) images and PlanetScope optical imagery covering the pre-disaster, post-disaster, and recovery phases (e.g., one week before and after the flood event) through Google Earth Engine (GEE). Preprocessing steps such as speckle filtering (to reduce noise), orthorectification (to correct geometric distortions), and calibration (to adjust for sensor inconsistencies) are applied to the SAR data to enhance water area identification (Filipponi, 2019). (b) Automatic segmentation uses thresholding on the SAR images to distinguish water bodies from non-water areas. The Otsu thresholding method creates binary images representing water and non-water regions (Otsu, 1979; Günen & Atasever, 2024). (c) Enhance the initial classifications using supervised classification techniques in PlanetScope data, supported by fuzzy logic to improve the delineation between land cover classes, such as vegetation, built-up areas, and water bodies, by handling the uncertainty in classification boundaries. (d) Post-process the classified images using morphological operations such as erosion and dilation to refine the flood maps. The accuracy of the results is validated by comparing the binary water masks derived from SAR data with reference water masks

created from high-resolution PlanetScope optical images, ensuring the robustness of the final flood extent maps. This study utilizes Sentinel-1 SAR and PlanetScope optical imagery, along with preliminary results from UNITAR-UNOSAT for comparison and validation. The results, derived from high-resolution Pleiades imagery, focus on assessing the immediate aftermath of the disaster, particularly the changes in land cover.

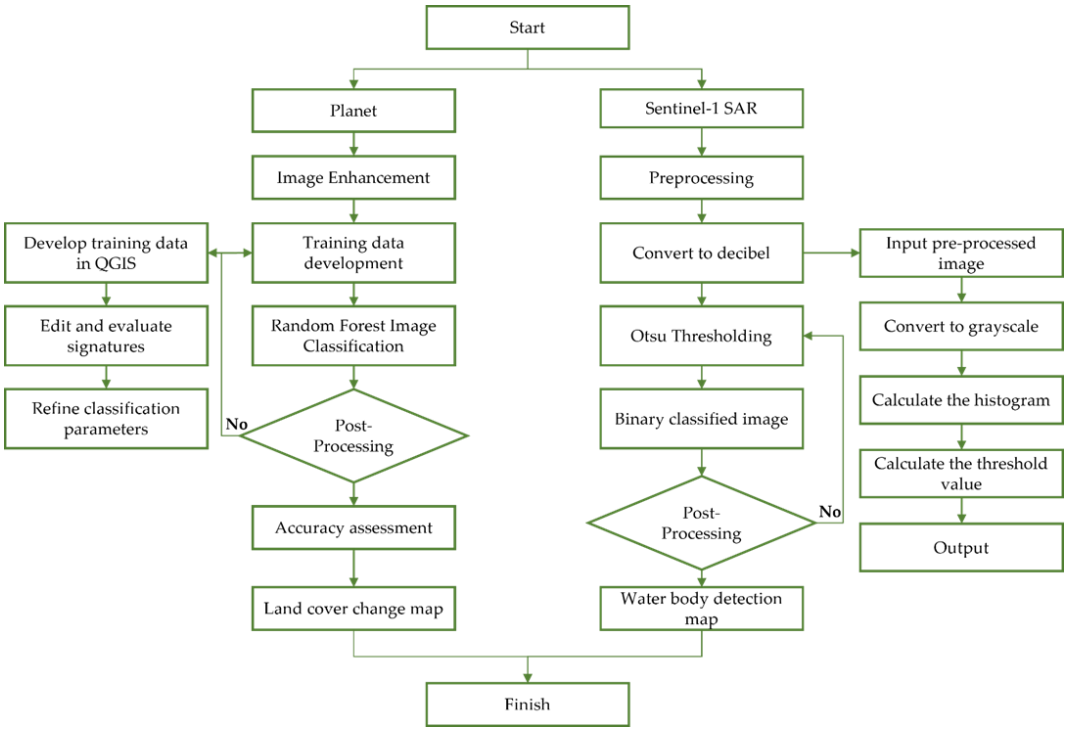

Figure 3: Flowchart of the study.

d. Image enhancement and training data development.

To enhance the imagery, we use both true-color and false-color band combinations. The true-color band combination (Red, Green, Blue) offers a natural representation of the land surface as perceived by the human eye. In contrast, the false-color band combination, which assigns near-infrared, red, and green bands to visible colors, effectively highlights vegetation health and water bodies. These band combinations facilitate a better interpretation of the data, as illustrated in Figure 4.

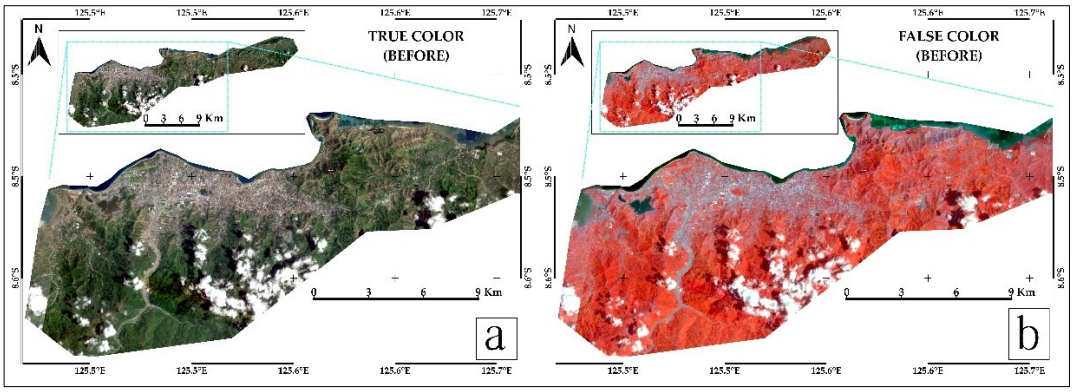

Figure 4: True and false color band combinations: (a) True color band combination, (b) False color band combination

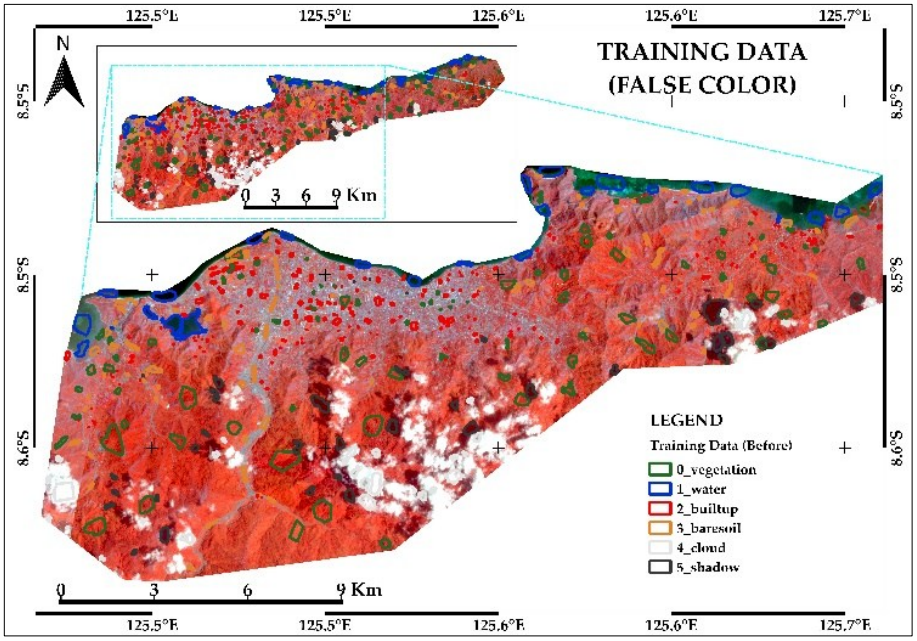

Figure 5: Training data development with false color base map

The training dataset is created by manually selecting regions of interest (ROIs) from the PlanetScope imagery, representing distinct land cover types such as vegetation, water, and built-up areas, as illustrated in Figure 5. The ROIs utilized in this research are 587, 619, and 600, corresponding to three distinct periods: pre-disaster, post-disaster, and recovery phase, respectively. These ROIs provide the spectral signatures to train the classification algorithm for identifying similar land cover types across the entire image. The training data are divided into two subsets to ensure reliable classification performance and reduce the risk of overfitting: 70% for training and 30% for validation.

This supervised classification approach collects training data by delineating areas representing different land cover types using polygons in QGIS. This data is imported into Google Earth Engine (GEE) as a feature collection. The algorithm uses the mean spectral signatures from the training sites to classify unlabeled pixels in the imagery, assigning each pixel to the most similar land cover class.

e. Random Forest Supervised Classification

The core of the land cover classification is performed using the Random Forest algorithm, a robust machine learning method known for its ability to handle high-dimensional and noisy data. The algorithm constructs multiple decision trees from the training data, where each tree makes a prediction. This ensemble approach helps reduce overfitting and improves model generalization (Kulkarni & Lowe, 2016; Akar & Güngör, 2012). The final classification is determined by majority voting across all trees in the forest. The Random Forest algorithm is applied using Google Earth Engine's ee.Classifier.smileRandomForest. For this study, 500 decision trees are used in the training process, striking a balance between model accuracy and computational efficiency.

The classification is based on six predefined land cover classes: Vegetation (0), Water (1), Built-up (2), Bare soil (3), Cloud (4), and Shadow (5). These predefined classes ensure consistency in the naming and labeling of the training data, which is essential for replicability and accuracy. This standardized classification scheme is crucial for maintaining accuracy and reliability across the dataset.

f. Morphological Operation and Accuracy Assessment

Morphological operations, such as erosion and dilation, are used to refine classified images. Erosion helps remove small, isolated misclassifications, while dilation enhances connected regions. These processes aim to reduce classification noise and eliminate minor misclassified areas (Akar & Güngör, 2012; Louverdis et al., 2002; Chudasama et al., 2015), especially around the boundaries across the land cover.

The classification is validated through an accuracy assessment, where a confusion matrix is generated to compare the classified land cover with the actual land cover, as indicated by ground-truth data collected from field surveys or high-resolution imagery. Metrics such as overall accuracy (the percentage of correctly classified pixels), user accuracy (the reliability of the classification for each class), producer accuracy (the probability that a certain class

is correctly represented), and Kappa statistics (a measure of agreement between the classification and ground-truth data) are calculated to ensure the reliability of the classification.

Morphological operations, such as erosion and dilation, are used to refine classified images. Erosion helps remove small, isolated misclassifications, while dilation enhances connected regions. These processes aim to reduce classification noise and eliminate minor misclassified areas (Priya & Kadhar Nawaz, 2017), especially around the boundaries across the land cover.

The classification is validated through an accuracy assessment, where a confusion matrix is generated to compare the classified land cover with the actual land cover, as indicated by ground-truth data collected from field surveys or high-resolution imagery. Metrics such as overall accuracy (the percentage of correctly classified pixels), user accuracy (the reliability of the classification for each class), producer accuracy (the probability that a certain class is correctly represented), and Kappa statistics (a measure of agreement between the classification and ground-truth data) are calculated to ensure the reliability of the classification.

Overall Accuracy measures the proportion of correctly classified instances (both true positives and true negatives) out of the total number of instances in the dataset, providing a general indication of the classification's performance (Nicolau et al., 2024).

Overall Accuracy (OA) is calculated using the formula:

$$Overall\ Accuracy\ (OA) = (TP + TN)/(TP + TN + FP + FN) \quad (1)$$

where TP is the number of true positives, TN is the number of true negatives, FP is the number of false positives, and FN is the number of false negatives.

Producer's Accuracy measures the percentage of correctly classified pixels for a particular class, relative to all the pixels that truly belong to that class (actual positives). This metric is important because it reflects how well the classification model identifies the actual occurrences of a given class (Nicolau et al., 2024).

Producer's Accuracy is calculated using the formula:

$$Producer's\ Accuracy\ (PA) = TP/(TP + FN) \quad (2)$$

where TP is the number of true positives (correctly classified pixels), and FN is the number of false negatives (pixels that were not classified as belonging to the class but actually do).

User's Accuracy, also known as Precision, measures the proportion of correctly classified pixels for a given class, relative to all pixels that were classified as belonging to that class.

This metric is important because it reflects how accurate the classification is for the predicted class (Nicolau et al., 2024).

User's Accuracy (UA) is calculated using the formula:

$$User's\ Accuracy\ (UA) = TP/(TP + FP) \quad (3)$$

where TP is the number of true positives (correctly classified pixels), and FP is the number of false positives (pixels that were incorrectly classified as belonging to the class but actually belong to a different class).

The Kappa Coefficient is a statistical measure of inter-rater agreement or classification accuracy that accounts for chance agreement (Nicolau et al., 2024). The Kappa statistic ranges from -1 to 1, with 1 indicating perfect agreement, 0 indicating chance-level agreement, and negative values showing disagreement worse than random chance. It is particularly useful for evaluating classification models, as it provides a more robust measure than overall accuracy, especially in situations where class imbalances may make overall accuracy misleading.

The Kappa Coefficient (k) is calculated using the formula:

$$k = (Po - Pe)/(1 - Pe) \quad (4)$$

Where:

- Po is the observed accuracy, which is the overall accuracy of the classification model
- Pe is the expected accuracy due to chance, calculated as:

$$Pe = \sum_{i=1}^{k} \left(\frac{(row_i \ x \ column_i)}{N^2} \right) \quad (5)$$

Here:

- ✓ N is the total number of samples,
- ✓ row_i is the sum of values in row iii of the confusion matrix,
- ✓ $column_i$ is the sum of values in column iii of the confusion matrix,
- ✓ and k is the total number of classes.

In GEE, Overall Accuracy represents the percentage of correctly classified pixels across all land cover types, providing a broad measure of the model's overall performance. User's Accuracy measures the proportion of correctly classified pixels for each class, indicating how reliable the classification is for a given land cover type. Producer's Accuracy assesses how well the model captures or identifies each land cover class, reflecting the completeness

of the classification for each class. The Kappa Coefficient adjusts for the possibility of chance agreement, providing a more refined measure of classification accuracy, with values closer to 1 indicating strong agreement.

These metrics are calculated in GEE (Nicolau et al., 2024) using confusionMatrix functions: Accuracy() for Overall Accuracy, consumersAccuracy() for User's Accuracy, producersAccuracy() for Producer's Accuracy, and kappa() for the Kappa Coefficient.

g. Binary segmentation with Otsu Thresholding

Otsu thresholding is a widely used image segmentation technique, particularly effective for distinguishing objects of interest, such as water bodies, from the background in grayscale images (Yousefi, 2015). In this study, Sentinel-1 SAR imagery is processed using Python libraries like rasterIO, OpenCV, NumPy, and Matplotlib. The Otsu method automatically determines the optimal threshold based on the histogram of pixel intensities, segmenting the image into water and non-water areas (Yousefi, 2015). The result is a binary image where water bodies are represented by pixel values of 1, and other areas by 0.

The segmentation process begins with preprocessing Sentinel-1 images using the European Space Agency's (ESA) SNAP software. SNAP ensures that the data is radiometrically and geometrically corrected, applying necessary operations such as orbit correction, calibration, and terrain correction to prepare the SAR data for accurate analysis. Once preprocessed in SNAP, the images are converted to the decibel (dB) scale to enhance the visibility of radar backscatter differences. Otsu's method is then applied to perform binary segmentation, simplifying the classification of water bodies for further analysis. The segmented images are exported in GeoTIFF format, preserving georeferencing information. These binary images are then imported into QGIS, where they are converted into vector files for precise waterline delineation.

Results

h. Land Cover Map

Using the Random Forest algorithm in Google Earth Engine (GEE), the land cover classification produced three maps: pre-disaster, post-disaster, and recovery phase. These maps classified the study area into six land cover types: vegetation, water, built-up areas, bare ground, clouds, and shadow. The results showed significant land cover changes due to the disaster, including widespread flooding, vegetation damage, and subsequent recovery

efforts. Figure 6 displays the pre-disaster map, showing extensive vegetation and built-up areas. Figure 7, the post-disaster map, reveals increased water bodies, reduced vegetation, and built-up regions due to flooding. Figure 8, the recovery phase map, shows partial vegetation and urban area restoration, with some regions experiencing regrowth while others still show bare ground.

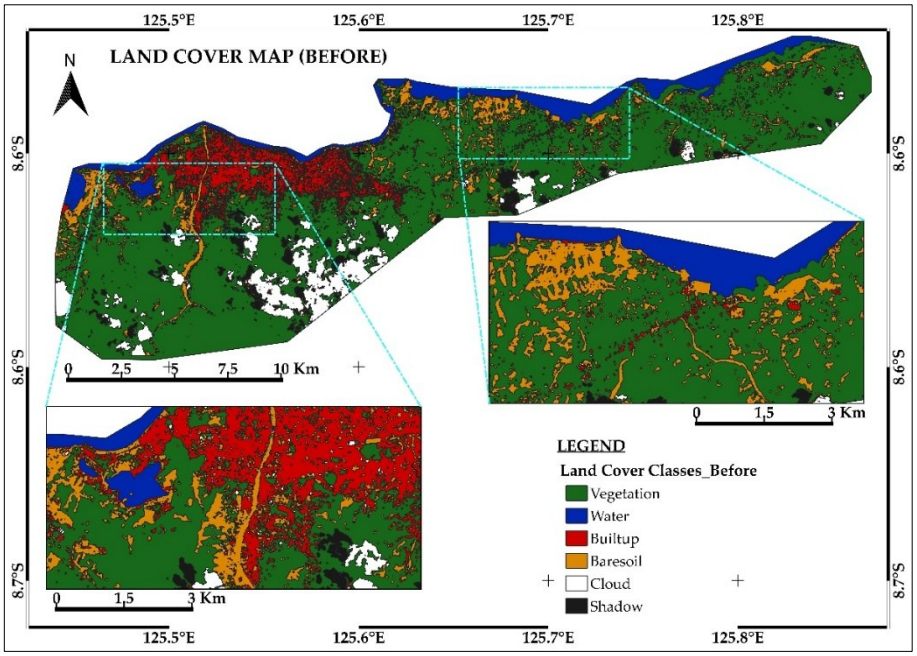

Figure 6: Land cover map of pre-disaster.

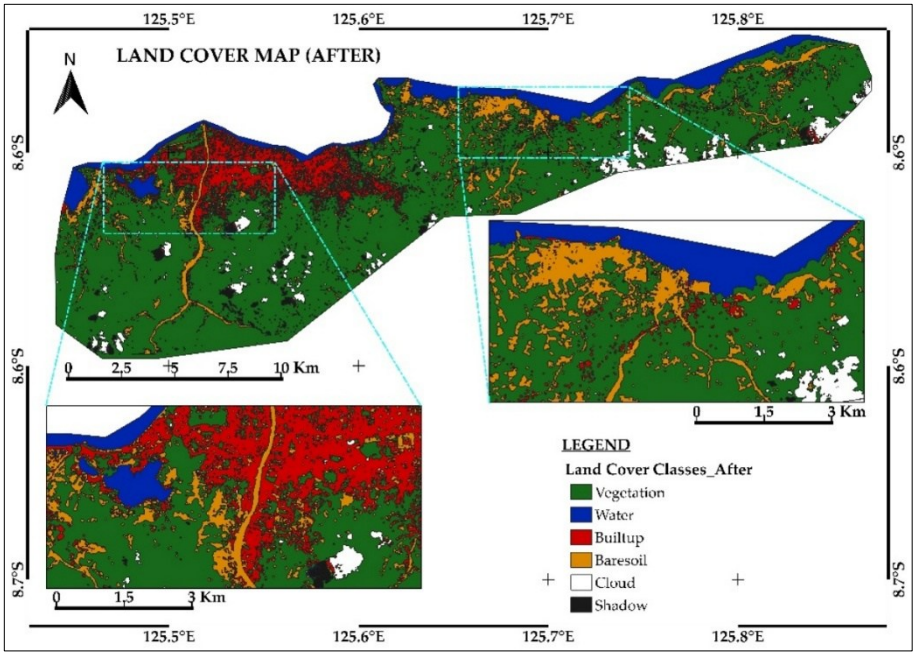

Figure 7: Land cover map of post-disaster.

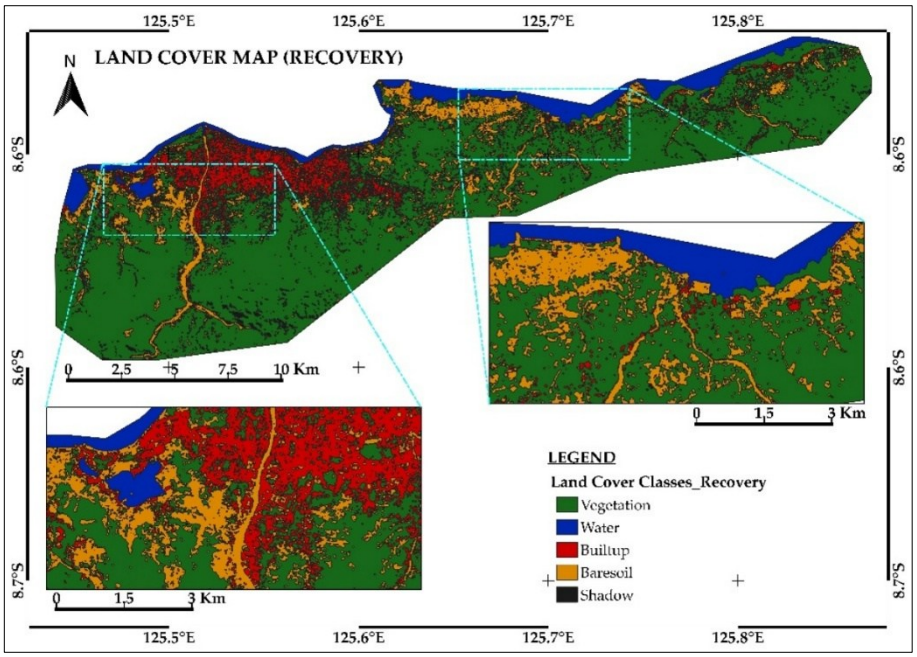

Figure 8: Land cover map of recovery phase.

i. Accuracy Assessment results

The confusion matrices from the pre-disaster, post-disaster, and recovery phases, as shown in Tables 3, 4, and 5, illustrate the evolution of land cover classification accuracy throughout the disaster management cycle. In the pre-disaster phase, the classification accuracy for vegetation is notably high, with 2,199 out of 2,237 pixels correctly classified, indicating robust baseline detection capabilities. However, the accuracy slightly decreased in the post-disaster phase, with 2,105 out of 2,132 vegetation pixels correctly classified, likely due to increased misclassification among shadow and cloud classes, which can be attributed to changes in the landscape and atmospheric conditions resulting from the disaster. By the recovery phase, the total number of pixels classified in each category diminishes, as seen with 2,177 out of 2,212 vegetation pixels correctly classified, reflecting the ongoing challenges and landscape alterations during recovery. These shifts highlight the dynamic nature of land cover in response to disaster events and underscore the importance of adaptive classification strategies to maintain accuracy over different phases.

Table 3: Confusion matrix of pre-disaster.

Confusion matrix (Pre-disaster)	Vegetation	Water	Built-up	Bare soil	Cloud	Shadow	Total
Vegetation	2199	0	0	8	1	29	2237
Water	1	1394	1	18	0	1	1415
Built-up	3	0	158	24	30	0	215
Bare soil	19	12	20	573	7	0	631
Cloud	1	0	18	9	537	0	565
Shadow	24	4	0	1	1	758	788
Total	2247	1410	197	633	576	788	5851

Table 4: Confusion matrix of post-disaster.

Confusion matrix (post-disaster)	Vegetation	Water	Built-up	Bare soil	Cloud	Shadow	Total
Vegetation	2105	0	2	15	6	4	2132
Water	1	1488	0	2	0	0	1491
Built-up	0	0	192	26	20	0	238
Bare soil	7	1	18	697	1	0	724
Cloud	8	0	7	1	453	0	469
Shadow	1	0	0	0	0	196	197
Total	2122	1489	219	741	480	200	5251

Table 5: Confusion matrix of recovery phase

Confusion matrix (recovery phase)	Vegetation	Water	Built-up	Bare soil	Cloud	Shadow	Total
Vegetation	2177	0	4	31	0	0	2212
Water	3	1470	0	16	0	0	1489
Built-up	0	1	157	42	0	0	200
Bare soil	14	2	26	721	0	0	763
Cloud	0	0	0	0	0	0	0
Shadow	2	0	0	0	0	43	45
Total	2196	1473	187	810	0	43	4709

Table 6 shows that the overall classification accuracy remains high throughout the disaster, with rates of 96.0% before the disaster, 97.7% after the disaster, and 97.0% during the recovery phase. The slight decrease in accuracy during recovery reflects the complexities

involved in land cover classification as the environment stabilizes; however, the model continues to perform robustly.

Table 6: Overall Accuracy

Overall Accuracy	Before	After	Recovery
	0.960	0.977	0.970

Further details from Tables 7 and 8 reveal variations in User's and Producer's Accuracies across different phases, with high accuracy observed for the vegetation and water classes. Notably, Cloud accuracy drops to zero during the recovery phase, indicating there were no cloud presence. The Kappa Index measures accuracy adjusted for random chance, showing the model's reliability with scores of 0.947, 0.968, and 0.954 in the pre-disaster, post-disaster, and recovery phases. This indicates consistent performance despite environmental changes**.**

Table 7: Confusion matrix of post-disaster.

Class	Before		After		Recovery	
	User's	Producer's	User's	Producer's	User's	Producer's
Vegetation	0.979	0.983	0.992	0.987	0.991	0.984
Water	0.989	0.985	0.999	0.998	0.998	0.987
Built-up	0.802	0.735	0.877	0.807	0.840	0.785
Bare soil	0.905	0.908	0.941	0.963	0.890	0.945
Cloud	0.932	0.950	0.944	0.966	0.000	0.000
Shadow	0.962	0.962	0.980	0.995	1.000	0.956

Table 8: Kappa Index

Kappa Index	Before	After	Recovery
	0.947	0.968	0.954

j. Land Cover Change Map

The Land Cover Change Map was generated using the Random Forest Algorithm on the Google Earth Engine (GEE) platform. The algorithm's outputs were subsequently imported into Quantum GIS (QGIS) for change detection analysis. Two images from different time periods were used to evaluate land cover changes. The Semi-Automatic Classification Plugin in QGIS was used for preprocessing, including atmospheric correction and resampling, to

ensure consistency between the images. The Land Cover Change tool was then applied to facilitate the analysis. In this analysis, the pre-disaster image serves as a reference for the initial classification, while the post-disaster image is used for the new classification. This approach is applied to compare changes between the pre-disaster and post-disaster phases, the post-disaster and recovery phases, and the pre-disaster and recovery phases. The comparison results are shown in Figures 9, 10, and 11.

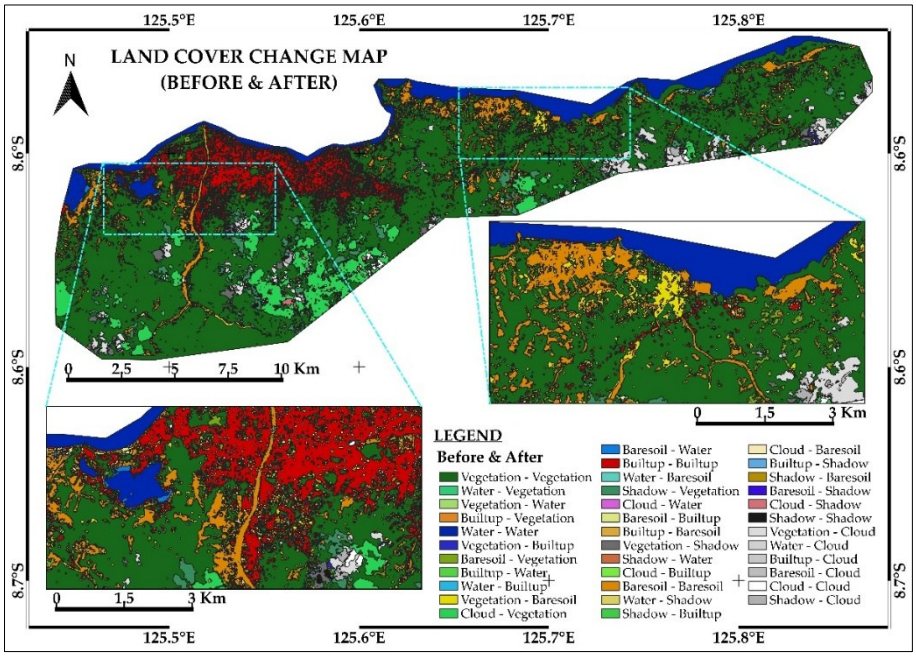

Figure 9: Land cover change map of pre-disaster and post-disaster

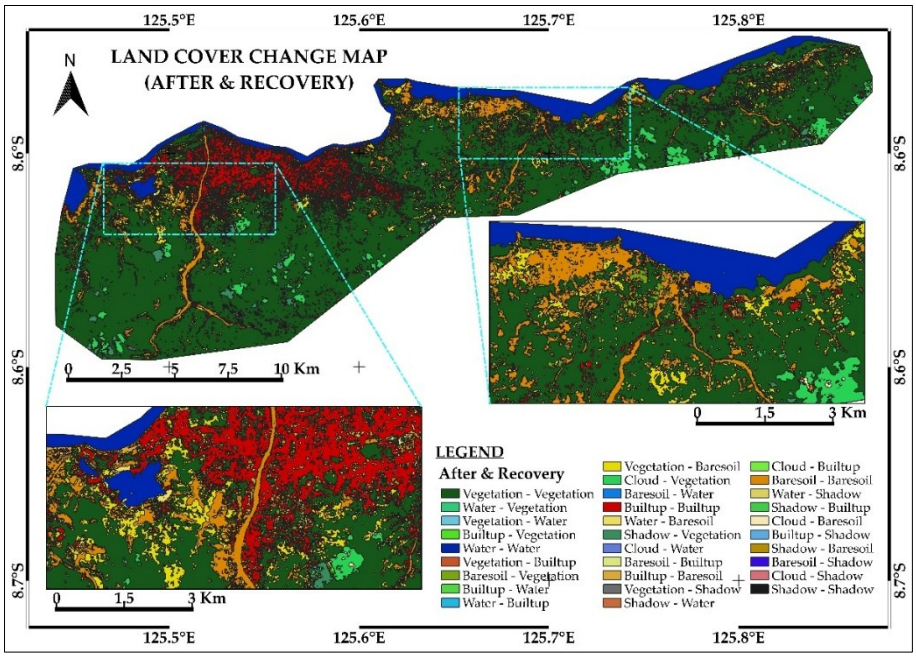

Figure 10: Land cover change map of post-disaster and recovery

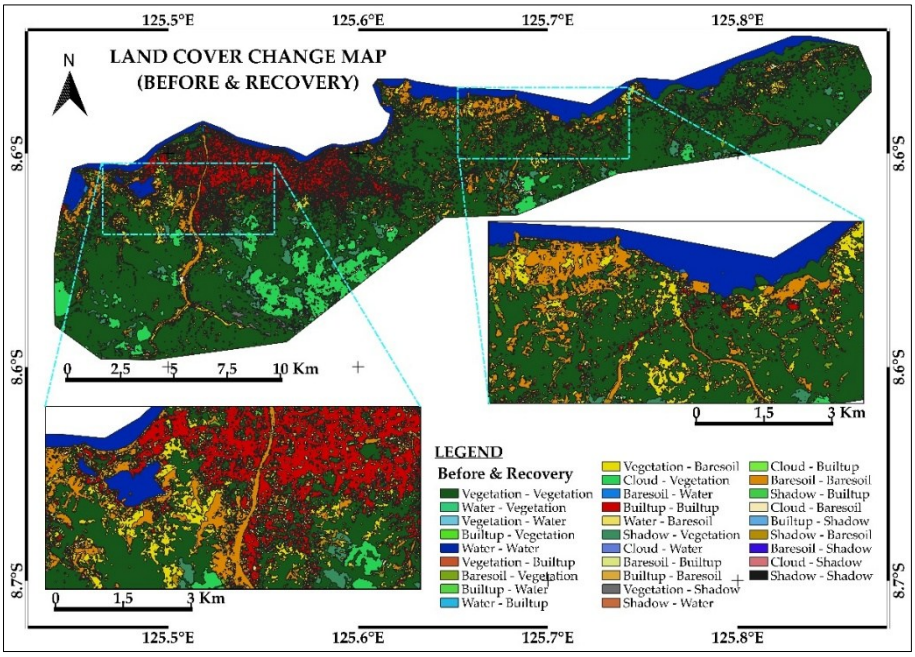

Figure 11: Land cover change map of pre-disaster and recovery phase

Figure 9, illustrates land cover changes in eastern Dili, with yellow areas indicating a shift from vegetation to bare soil. This reflects a significant loss of agricultural land due to flooding and river overflows that washed away the vegetation area. Additionally, the light blue area near Lake Tasi-Tolu shows an increase in the lake's volume post-disaster, as it absorbed considerable floodwater, affecting nearby communities.

Figure 10 illustrates the recovery phase, showing significant vegetation regrowth in the light green areas, indicating that vegetation is returning after the disaster. Meanwhile, the decrease in the lake's water volume, reflected by the reduced light-yellow color, suggests a return to pre-disaster levels or effective response measures.

Figure 11 indicates that some vegetation did not fully recover after the disaster, as shown by the comparison of land cover classifications before and during recovery. This suggests that sediment from river overflow completely covered certain plants and crops.

Furthermore, these results can be seen in Figure 12, which illustrates the area of the land cover classes. Vegetation slightly increases post-disaster but declines during recovery, while water areas follow a similar pattern. Built-up areas continue to grow, though some may result from misclassification with bare soil due to the similarities in pixel values. Cloud cover as well as shadow significantly decreases after the disaster.

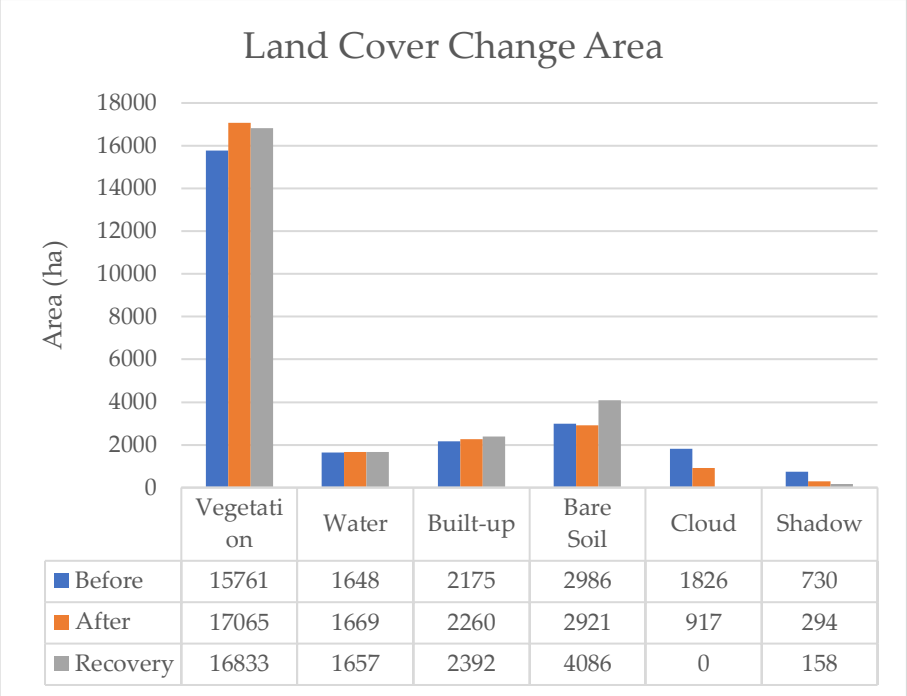

	Vegetation	Water	Built-up	Bare Soil	Cloud	Shadow
Before	15761	1648	2175	2986	1826	730
After	17065	1669	2260	2921	917	294
Recovery	16833	1657	2392	4086	0	158

Figure 12: Statistical values for land cover change between three different periods.

k. Water body detection map with SAR Imagery

Water Body Detection Map: Binarized images represent water bodies, where water is indicated by pixel values of 1 and non-water areas by 0. These images are loaded into QGIS for waterline extraction and delineation. Comparisons with Google satellite imagery or other high-resolution satellite data enhance the accuracy of the waterline selection in vector files. Figures 13, 14, and 15 display the delineated waterline of Lake Tasi-Tolu in Dili during the pre-disaster, post-disaster, and recovery phases, respectively, marked by yellow lines. Figure 16 presents the statistics detailing changes in water class area across these periods, calculated by extracting the waterline area from the classified image.

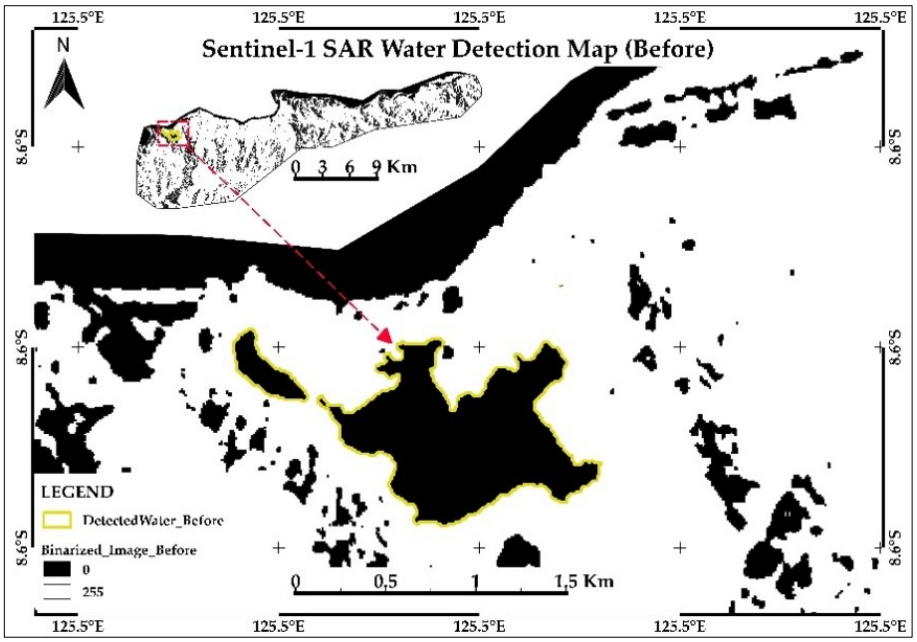

Figure 13: Water detection for pre-disaster with Sentinel-1 SAR image

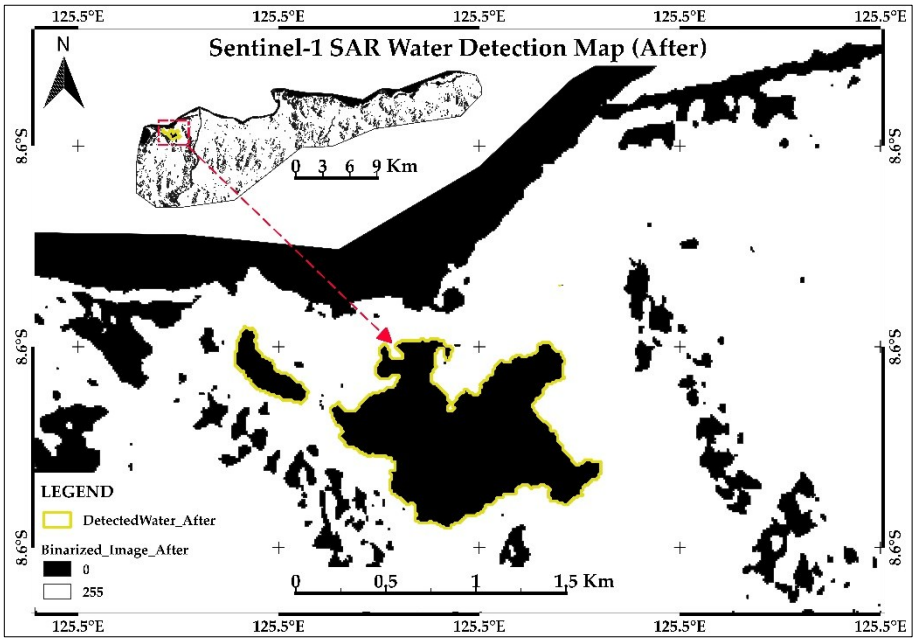

Figure 14: Water detection for post-disaster with Sentinel-1 SAR image

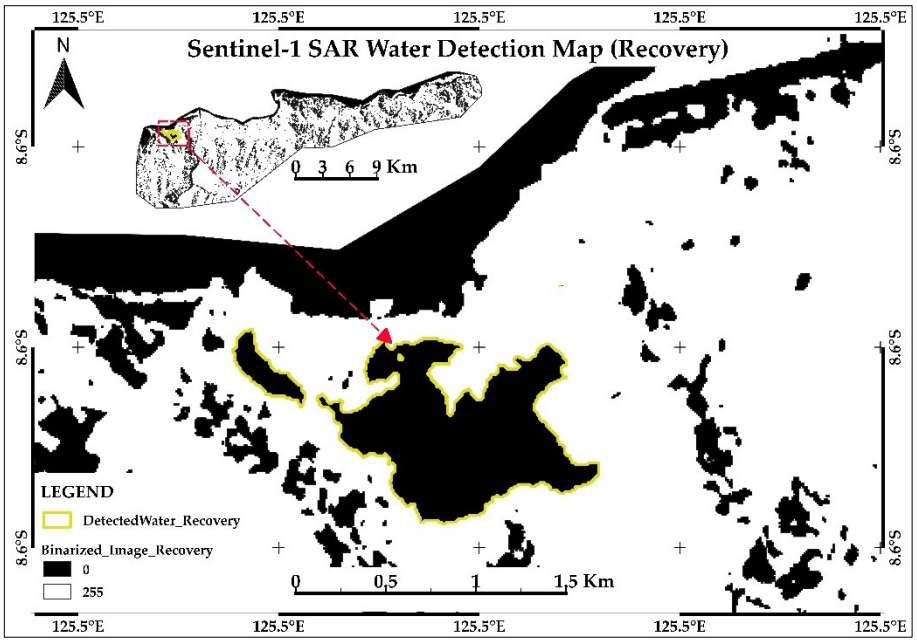

Figure 15: Water detection for recovery phase with Sentinel-1 SAR image

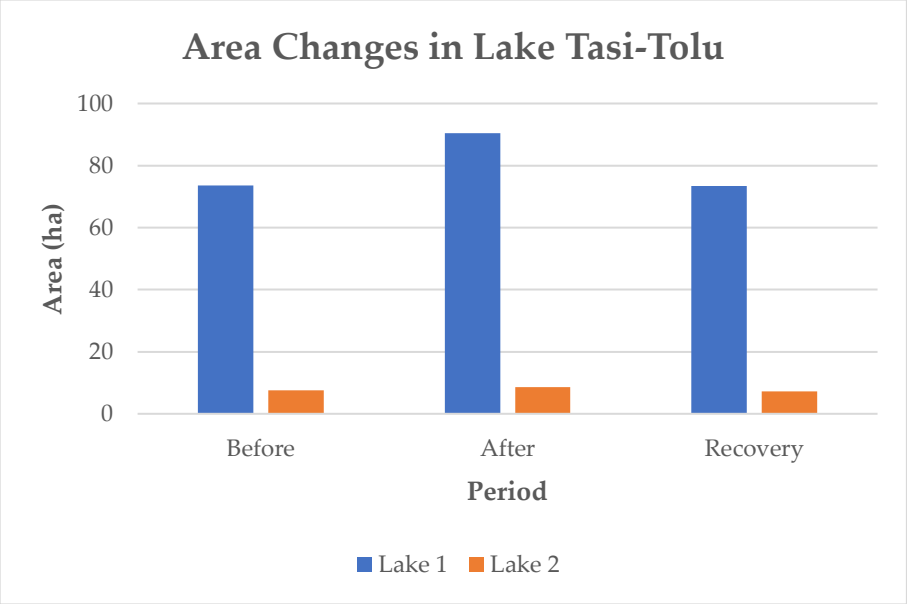

Figure 16: Water area in Tasi-Tolu Lake extracted using Planet Image classification results.

l. Visual Correlation between SAR and Optical results

The water detection results from land cover change detection using PlanetScope imagery and binary-segmented Sentinel-1 imagery was combined to visualize the differences between the two datasets. In Figures 17, 18, and 19, blue indicates water detection in the

optical (PlanetScope) imagery, while red indicates water detection in the Sentinel-1 SAR imagery.

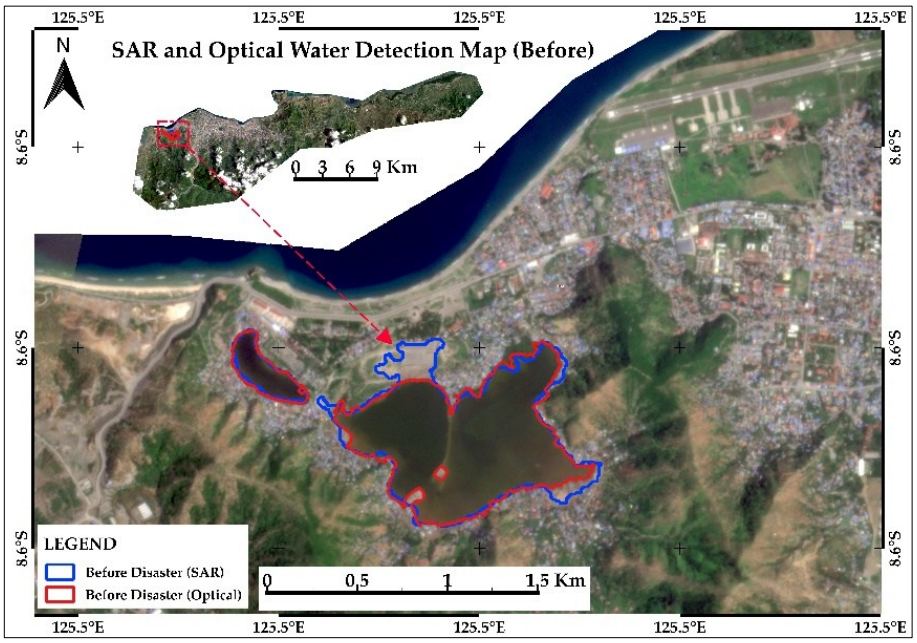

Figure 17: Overlay of waterline detection in Lake Tasi-Tolu using both Optical and SAR classification results for pre-disaster.

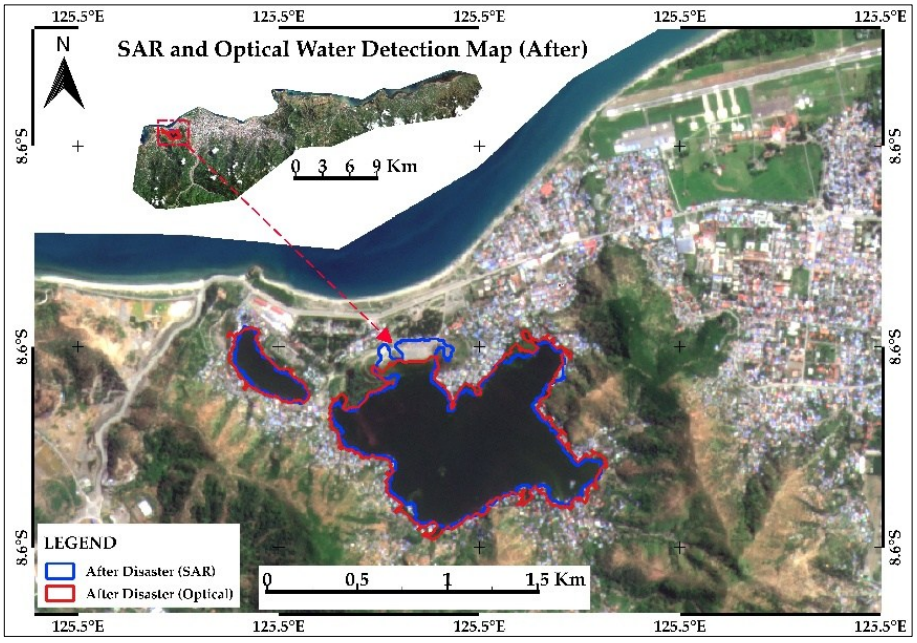

Figure 18: Overlay of waterline detection in Lake Tasi-Tolu using both Optical and SAR classification results for post-disaster.

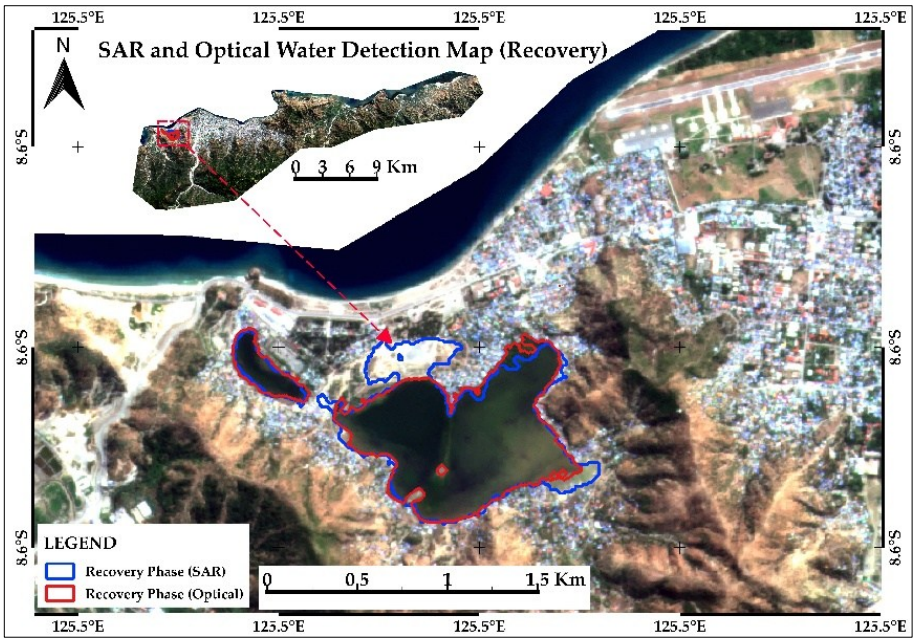

Figure 19: Overlay of waterline detection in Lake Tasi-Tolu using both Optical and SAR classification results for recovery phase.

m. Visualization validation with Preliminary Results by Disaster Charter (UNITAR/UNOSAT)

Figures 20a and 20b present preliminary results from UNITAR-UNOSAT, which used Pleiades imagery to assess the aftermath of the disaster in Timor-Leste (International Disasters Charter, 2021). Their analysis highlighted regions most impacted by flooding, focusing on changes in land cover, such as water bodies, bare soil, and built-up areas. These early results, derived from high-resolution optical imagery, provided a visible assessment of the immediate changes caused by the disaster. The Figures 20c and 20d show the classification results from this study, capturing similar patterns of change, such as landslides and vegetation loss due to flooding. A strong correlation exists between the two analyses, as both consistently identify severely affected areas.

The Random Forest classification using PlanetScope data in this study further validates the preliminary findings, offering a more automated and scalable method for detecting land cover changes. The observed decrease in vegetation and the increase in water and bare soil confirm the reliability of this approach, aligning with established methodologies such as those used by UNITAR-UNOSAT. This consistency underscores the effectiveness of combining high-resolution satellite imagery with machine-learning algorithms for practical disaster assessment and recovery monitoring.

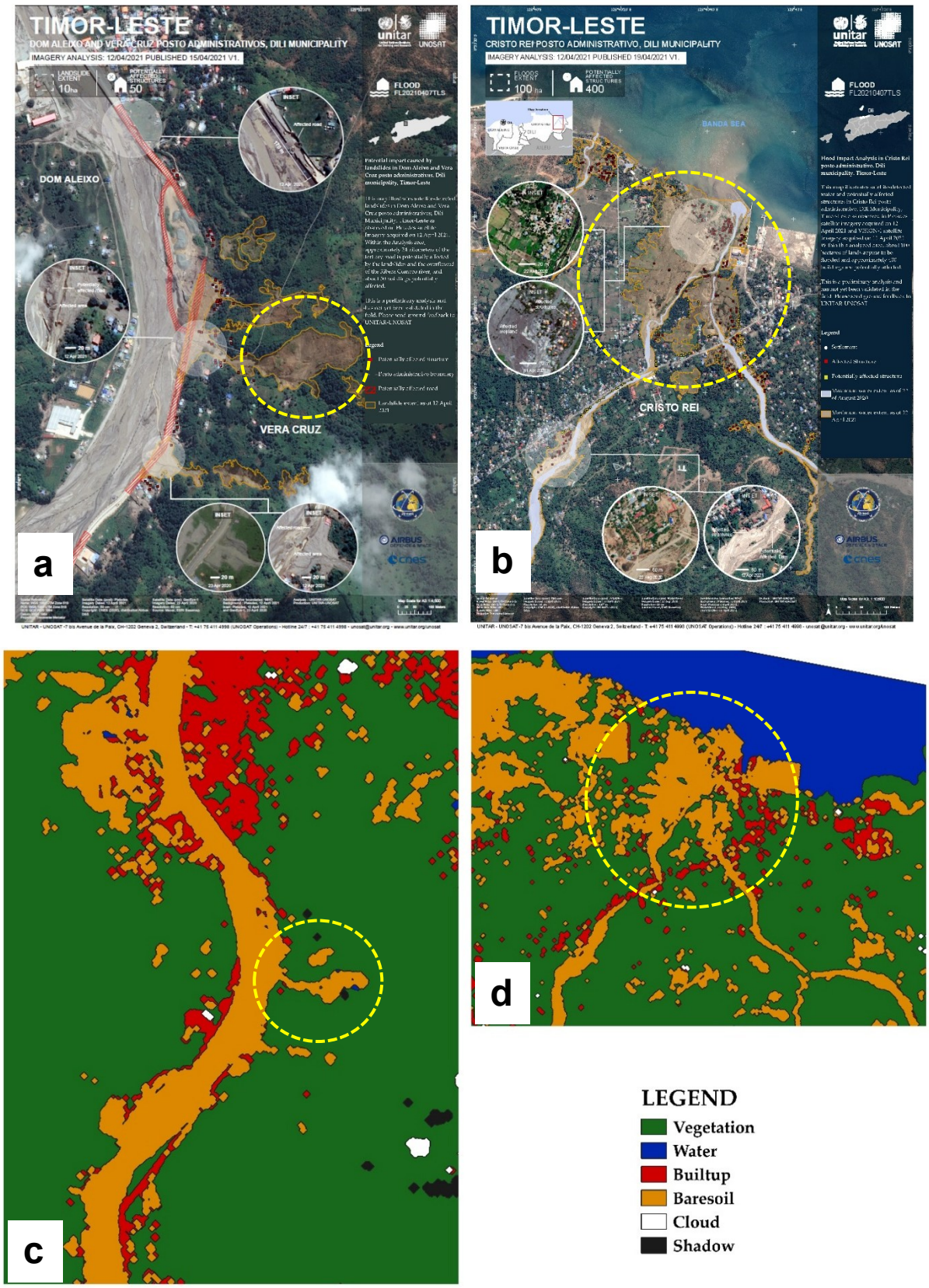

Figure 20: Preliminary results provided by UNITAR-UNOSAT immediately after the disaster using Pleiades satellite imagery: (a) Landslide detected by Pleiades satellite, (b)

Vegetation loss detected by Pleiades satellite, (c) Landslide detected by classification results, (d) Vegetation loss detected by classification results.

n. Morphological Operation

In this paper, we derived the training data through visual interpretation of high-resolution PlanetScope satellite imagery. Generating this training data required local knowledge to ensure accurate representation, which was then used to feed the Random Forest Supervised Classification Algorithm. The classification results exhibited 'salt-and-pepper' noise, caused by spectral variability in the imagery, despite the high overall accuracy. We perform the morphological analyses to deal with the noise, and the results demonstrate a better corrected version of the classification results as depicted in Figure 21. Nevertheless, the overall accuracy provided a strong representation of the land cover classification results for the pre-disaster, post-disaster, and recovery phases, with accuracies of 96%, 97.7%, and 97%, respectively.

The role of SAR imagery in this study primarily focuses on detecting the water extent in the lake, as this location was identified as one of the inundated areas during the heavy rainfall. SAR technology is capable of detecting water regardless of weather conditions. The binary segmentation results revealed a significant change in water volume by comparing the waterline size across the three images.

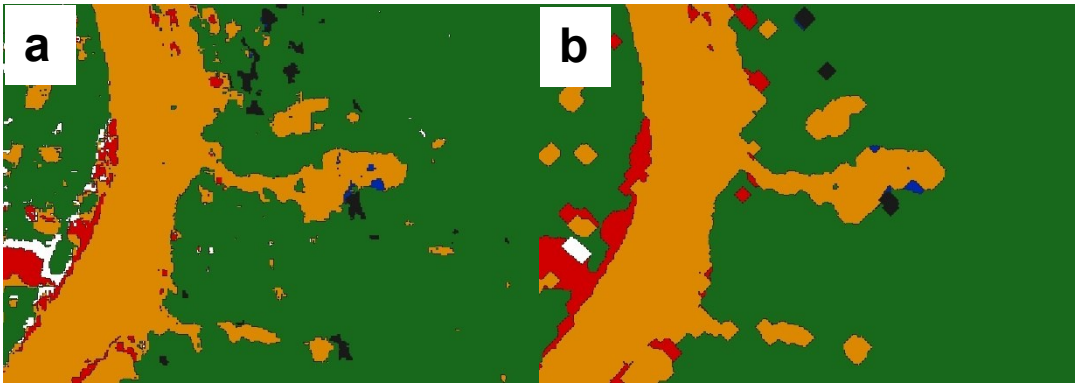

Figure 21: Morphological operation after the classification results: (a) Noises present in the classified image; (b) Noise corrected using the dilation approach.

Conclusion

A Random Forest workflow implemented in Google Earth Engine reliably characterized disaster-related land-cover dynamics across pre-disaster, post-disaster, and recovery phases when trained on curated reference data for vegetation, water, built-up, bare soil, cloud, and

shadow. The resulting phase-specific maps captured the anticipated flooding signal and its aftermath: post-disaster imagery indicated expanded water extent and reduced vegetative cover, followed by partial regrowth and urban re-establishment during recovery.

Classification performance remained consistently strong throughout all phases. Overall accuracies were 96.0 percent for pre-disaster, 97.7 percent for post-disaster, and 97.0 percent for recovery, with Kappa indices of 0.947, 0.968, and 0.954, respectively. These results indicate high agreement beyond chance and stable model behavior despite substantial scene changes. The accuracy of class-level users and producers was particularly high for vegetation and water classes across all phases.

Change analysis supported the classification results. Post-disaster comparisons highlighted the conversion of vegetation to bare soil and the increase in open water in eastern Dili, including the Tasi-Tolu area. Recovery-phase comparisons revealed significant vegetation regrowth and a reduction in water areas toward pre-event conditions, although some locations remained degraded. These patterns were evident in the phase-to-phase change maps and associated statistics.

The integration of Sentinel-1 SAR data with optical results increased the robustness of open-water detection under cloudy conditions. Binary segmentation of SAR imagery enabled clear delineation of waterlines around Lake Tasi-Tolu across all three phases. Overlays of SAR-derived and optical-derived water masks demonstrated strong spatial correspondence, reinforcing the reliability of water extent estimates during and after the flood.

Final post-classification morphological processing effectively suppressed salt-and-pepper noise resulting from spectral heterogeneity, producing cleaner thematic outputs without altering the interpretation of phase-specific land-cover trajectories.

o. Limitations and future work

- ✓ **Reference data provenance and coverage.** Training samples were derived from visual interpretation and local knowledge. While effective, this approach can introduce interpreter bias and may not fully represent within-class variability in all areas. Future work should expand training coverage and, where possible, incorporate field or very-high-resolution reference data.
- ✓ **Class confusion in spectrally similar surfaces.** The results indicate potential confusion between built-up and bare soil in some areas due to similar reflectance,

which may inflate apparent urban gains. Incorporating additional texture features, multi-temporal composites, or SAR backscatter metrics could help distinguish these classes.

- ✓ **Cloud/shadow dynamics and phase comparability.** Post-disaster conditions led to increased interactions with shadow/cloud classes in certain areas, and the recovery phase had no cloud presence in the evaluation subset. While the overall conclusions remain consistent, phase-to-phase accuracy can be influenced by these atmospheric/illumination differences; stratified sampling and cloud-shadow harmonization would further stabilize comparisons.
- ✓ **Binary water detection thresholds.** SAR-based water masks relied on simple binary segmentation. Threshold selection can significantly impact shoreline placement, particularly in shallow or vegetated waters. Adaptive thresholding and the use of ancillary elevation or slope constraints could refine waterline delineation.

Collectively, the findings provide an evidence base for mapping flood impacts and monitoring recovery using high-resolution PlanetScope imagery, complemented by Sentinel-1 SAR. Addressing the limitations above—particularly broader, more systematic reference data and enhanced class-separation strategies—will further improve transferability and operational reliability in future applications.

References

Akar, Ö., & Güngör, O., (2012). Classification of Multispectral Images Using Random Forest Algorithm. Journal of Geodesy and Geoinformation, 1(2), 105–112. https://doi.org/10.9733/jgg.241212.1

Al Shafian, S., & Hu, D., (2024). Integrating Machine Learning and Remote Sensing in Disaster Management: A Decadal Review of Post-Disaster Building Damage Assessment. Buildings, 14, 2344. https://doi.org/10.3390/buildings14082344

Chudasama, D., Patel, T., Joshi, S., & Prajapati, G. I., (2015). Image Segmentation Using Morphological Operations. International Journal of Computer Applications, 117(18), 16–19.

Emanuel, K. (2005). Increasing destructiveness of tropical cyclones over the past 30 years. Nature, 436, 686–688. https://doi.org/10.5120/20654-3197

Filipponi, F., (2019). Sentinel-1 GRD Preprocessing Workflow. Proceedings, 18, Article 11. https://doi.org/10.3390/ECRS-3-06201

Gómez, C., White, J. C., & Wulder, M. A., (2016). Optical Remotely Sensed Time Series Data for Land Cover Classification: A Review. ISPRS Journal of Photogrammetry and Remote Sensing, 116, 55–60. https://doi.org/10.1016/j.isprsjprs.2016.03.008

Government of Timor-Leste, United Nations, & World Bank., (2021, October). Post Disaster Needs Assessment: Tropical Cyclone Seroja and the Easter Flood April 2021, Executive Summary.

Gu, Z., & Zeng, M., (2024). The Use of Artificial Intelligence and Satellite Remote Sensing in Land Cover Change Detection: Review and Perspectives. Sustainability, 16, 274. https://doi.org/10.3390/su16010274

Günen, M. A., & Atasever, U. H., (2024). Remote Sensing and Monitoring of Water Resources: A Comparative Study of Different Indices and Thresholding Methods. Science of the Total Environment, 926, 172117. https://doi.org/10.1016/j.scitotenv.2024.172117

International Disasters Charter., (2021, April 4). Tropical Cyclone Seroja in Timor-Leste – Activation 701. Retrieved September 30, 2024, from https://disasterscharter.org/es/web/guest/activations/-/article/flood-large-in-timor-leste-activation-701-

Jing, R., Heft-Neal, S., Chavas, D. R., Griswold, M., Wang, Z., Clark-Ginsberg, A., Guha-Sapir, D., Bendavid, E., & Wagner, Z. (2024). Global population profile of tropical cyclone exposure from 2002 to 2019. Nature, 626, 549–550. https://doi.org/10.1038/s41586-023-06963-z

Klotzbach, P. J., Wood, K. M., Schreck III, C. J., Bowen, S. G., Patricola, C. M., & Bell, M. M. (2022). Trends in global tropical cyclone activity: 1990–2021. Geophysical Research Letters, 49, e2021GL095774. https://doi.org/10.1029/2021GL095774

Kulkarni, A. D., & Lowe, B., (2016). Random Forest Algorithm for Land Cover Classification. International Journal on Recent and Innovation Trends in Computing and Communication, 4(3), 58–63. https://scholarworks.uttyler.edu/compsci_fac/1

Lang, F., Zhu, Y., Zhao, J., Hu, X., Shi, H., Zheng, N., & Zha, J., (2024). Flood Mapping of Synthetic Aperture Radar (SAR) Imagery Based on Semi-Automatic Thresholding and Change Detection. Remote Sensing, 16, 2763. https://doi.org/10.3390/rs16152763

Louverdis, G., Vardavoulia, M. I., Andreadis, I., & Tsalides, Ph., (2002). A New Approach to Morphological Color Image Processing. Pattern Recognition, 35, 1733–1741. https://doi.org/10.1016/S0031-3203(01)00166-2

Mashala, M. J., Dube, T., Mudereri, B. T., Ayisi, K. K., & Ramudzuli, M. R., (2023). A Systematic Review on Advancements in Remote Sensing for Assessing and Monitoring Land

Use and Land Cover Changes Impacts on Surface Water Resources in Semi-Arid Tropical Environments. Remote Sensing, 15, 3926. https://doi.org/10.3390/rs15163926

Nicolau, A. P., Dyson, K., Saah, D., & Clinton, N., (2024). Accuracy Assessment: Quantifying Classification Quality. In Cardille, J. A., et al. (Eds.), Cloud-Based Remote Sensing with Google Earth Engine, 135–145. https://doi.org/10.1007/978-3-031-26588-4_7

Otsu, N., (1979). A Threshold Selection Method from Gray-Level Histograms. IEEE Transactions on Systems, Man, and Cybernetics, 9(1), 62–66. https://doi.org/10.1109/TSMC.1979.4310076

Parra, L. (2022). Remote sensing and GIS in environmental monitoring. Applied Sciences, 12, 8045. https://doi.org/10.3390/app12168045

Pickering, J., Tyukavina, A., Khan, A., Potapov, P., Adusei, B., Hansen, M. C., & Lima, A., (2021). Using Multi-Resolution Satellite Data to Quantify Land Dynamics: Applications of PlanetScope Imagery for Cropland and Tree-Cover Loss Area Estimation. Remote Sensing, 13, 2191. https://doi.org/10.3390/rs13112191

Priya, M. S., & Kadhar Nawaz, G. M., (2017). Effective Morphological Image Processing Techniques and Image Reconstruction. International Journal of Trend in Research and Development (IJTRD), Special Issue, 18–22. https://www.ijtrd.com/papers/IJTRD8373.pdf

Tiampo, K. F., Huang, L., Simmons, C., Woods, C., & Glasscoe, M. T., (2022). Detection of Flood Extent Using Sentinel-1A/B Synthetic Aperture Radar: An Application for Hurricane Harvey, Houston, TX. Remote Sensing, 14, 2261. https://doi.org/10.3390/rs14092261

Umam, C., Pranowo, W. S., Azhari, F., Hendra, Setiyadi, J., & Aji, T. (2024). Analysis of influence of Cyclone Seroja on wave height and tide in the Indian Ocean. Omni-Akuatika, 20(1), 38–49. http://dx.doi.org/10.20884/1.oa.2024.20.1.1114

Vickers, H., Malnes, E., & Høgda, K.-A., (2019). Long-Term Water Surface Area Monitoring and Derived Water Level Using Synthetic Aperture Radar (SAR) at Altevatn, a Medium-Sized Arctic Lake. Remote Sensing, 11, 2780. https://doi.org/10.3390/rs11232780

Wang, R., Sun, Y., Zong, J., Wang, Y., Cao, X., Wang, Y., Cao, X., Wang, Y., Cheng, X., & Zhang, W. (2024). Remote sensing application in ecological restoration monitoring: A systematic review. Remote Sensing, 16, 2204. https://doi.org/10.3390/rs16122204

World Bank Group, & Asian Development Bank. (2021). Climate risk country profile: Timor-Leste. World Bank.

Yousefi, J., (2015, May). Image Binarization Using Otsu Thresholding Algorithm. Research. https://doi.org/10.13140/RG.2.1.4758.9284